This is a repository copy of *Multiresolution eXtended Free-Form Deformations (XFFD) for non-rigid registration with discontinuous transforms.*.

Article:

Multiresolution eXtended Free-Form Deformations (XFFD) for Non-rigid Registration with Discontinuous Transforms

Rui Hua, Jose M. Pozo, Zeike A. Taylor, Alejandro F. Frangi

Center for Computational Imaging and Simulation Technologies in Biomedicine (CISTIB)
The University of Sheffield, Sheffield, United Kingdom.

Abstract

Image registration is an essential technique to obtain point correspondences between anatomical structures from different images. Conventional non-rigid registration methods assume a continuous and smooth deformation field throughout the image. However, the deformation field at the interface of different organs is not necessarily continuous, since the organs may slide over or separate from each other. Therefore, imposing continuity and smoothness ubiquitously would lead to artifacts and increased errors near the discontinuity interface.

In computational mechanics, the eXtended Finite Element Method (XFEM) was introduced to handle discontinuities without using computational meshes that conform to the discontinuity geometry. Instead, the interpolation bases themselves were enriched with discontinuous functional terms. Borrowing this concept, we propose a multiresolution eXtented Free-Form Deformation (XFFD) framework that seamlessly integrates within and extends the standard Free-Form Deformation (FFD) approach. Discontinuities are incor-

porated by enriching the B-spline basis functions coupled with extra degrees of freedom, which are only introduced near the discontinuity interface. In contrast with most previous methods, restricted to sliding motion, no ad hoc penalties or constraints are introduced to reduce gaps and overlaps. This allows XFFD to describe more general discontinuous motions. In addition, we integrate XFFD into a rigorously formulated multiresolution framework by introducing an exact parameter upsampling method.

The proposed method has been evaluated in two publicly available datasets: 4D pulmonary CT images from the DIR-Lab dataset and 4D CT liver datasets. The XFFD achieved a Target Registration Error (TRE) of 1.17 ± 0.85 mm in the DIR-lab dataset and 1.94 ± 1.01 mm in the liver dataset, which significantly improves on the performance of the state-of-the-art methods handling discontinuities.

1. INTRODUCTION

Medical image registration aims at establishing point correspondences between anatomical structures in different images. Accurate correspondences are relied upon by a wide range of clinical applications. One of special relevance is registration of temporal image sequences, such as motion analysis and monitoring disease development in longitudinal studies. One of the most widely used non-rigid registration frameworks is Free-Form Deformations (FFDs) (Rueckert et al., 1999). FFDs are versatile and computationally

Email address: rui.hua@sheffield.ac.uk (Rui Hua)

efficient, with multiple extensions, such as, multiresolution (Rueckert et al., 1999), multiview (Piella et al., 2013), spatio-temporal (De Craene et al., 2012), and diffeomorphic registration (Rueckert et al., 2006).

Classical FFD methods commonly rely on B-spline transformations, resulting in smooth and continuous deformation fields, which reflect the similarly smooth deformation hypothesised to be exhibited by compliant tissues. This constraint, however, is not desirable when the tissue transitions are discontinuous. For instance, discontinuities are present at the interface of structures that undergo different motion patterns during the respiratory cycle, such as, the lungs and the thoracic cage. For images acquired in different pose, the relative position between different organs can also change, as observed in the abdominal organs. In longitudinal studies, discontinuities may also result from morphological changes associated with growth processes or treatments, such as at the boundaries between tumours and surrounding parenchyma. Artificially imposing continuity in registration of tissues that exhibit discontinuities can introduce artifacts, resulting in non-physically plausible deformation and strain fields (Fig. 4). The strain is related to the physical properties of tissues, which are key to many diagnostic questions (Mirsky, 1976). Therefore, artifacts leading to incorrect strain field have a direct negative impact on the assessment of kinetics and functionality of the corresponding organs.

1.1. *Previous works*

Proper management of physical discontinuities in medical image registration is therefore an active area of research. According to the transformation model employed, the existing approaches can be classified into two

categories; diffusion- or spline-based registration methods. In most diffusion-based methods, discontinuities were explicitly incorporated in the regularization schemes. Direction-dependent regularizers were employed by decomposing the deformation field into normal and tangential directions at the discontinuity interface and smoothing was only applied in the tangential components but not across the boundary (Schmidt-Richberg et al., 2012; Pace et al., 2013). Locally adaptive regularizers were adopted with discontinuity preserving properties (Ruan et al., 2009; Papież et al., 2014).

FFDs are parametric transformation models with fewer degrees of freedom; thus, they are potentially more efficient. They naturally produce smooth deformation fields without explicit regularizers. The basis functions are piece-wise polynomial and have local support, so that they are computationally efficient and compatible with gradient-based optimizers. The most straightforward FFD-based method for handling discontinuities is based on registering regions on either side of a discontinuity independently using masks, covering the object of interest. However, this simple approach does not prevent the misalignment of the object boundaries. In the transformed image, the organ can shrink or expand beyond the actual boundary position, since it is not penalized by the cost function, unless specific constraints are imposed.

Wu et al. (2008) addressed this problem by using the region masks to modify the image intensities outside the region to a homogenous extreme value. Thus, any misalignment is penalized since it increases the dissimilarity metric. This method requires provision of masks for both moving and target image. This requirement is reduced to one discontinuity interface for the

target image in (Delmon et al., 2013). They introduced another strategy based on the decomposition of the displacement field into the normal and tangential directions of the interface in a multiple B-spline transformation framework. The main issue of this method is that the decomposition into the tangential and normal directions was performed at the control points. Thus, the interpolation of these directions only approximates the orientation of the actual discontinuity surface, producing inaccuracies in the registration results. This problem is more evident when there are structures of smaller scale, like sharp edges present in the interface delimiting the lungs. In their experiments, they used a motion mask covering also the abdomen, based on the assumption that the lungs and the abdomen move continuously together, although this assumption is not accurate, as the lungs and the abdominal organs slide relative to each other (Pace et al., 2011). This restriction in the shape of the discontinuity interface was alleviated by using multiple B-spline transformations covering the regions separated by the discontinuity interface, and a penalty term to reduce gaps and overlaps at the region boundaries (Berendsen et al., 2014).

Most of the existing registration methods handling discontinuities are tailored solely to sliding motion. This type of discontinuity exists between structures which are adjoint and unable to get detached, but which are able to slide over each other. This assumption concerning the allowed motion is not suitable for some organs undergoing more complex motion. For instance, the liver slides over the diaphragm and some other abdominal organs, but it also touches and separates from some organs, such as the kidney. We refer to this type of motion as free discontinuous motion, existing between

5

objects that are not attached and can move freely from each other. Imposing a sliding constraint at the interface of organs detaching from each other can introduce detrimental artifacts in the deformation field.

1.2. *Our contribution*

In this work, we present a novel method for treating discontinuities in general, coined eXtended Free Form Deformation (XFFD). The XFFD method was inspired by the interpolation function enrichment concepts that underpin eXtended Finite Element Methods (XFEMs) and Partition of Unity Methods more generally. The XFEM is an extension of Finite Element Methods (FEM) aiming at handling discontinuities without the need of remeshing, which is employed to adapt the finite element mesh by tracking the discontinuities at each time point. We have borrowed the enrichment concept from XFEM, extended it from the linear interpolation case to that of cubic B-splines, and incorporated it into the FFD formalism. In XFFD, discontinuities are incorporated in the enrichment term with extra degrees of freedom within a single B-spline transformation.

FFD registration algorithms often employ a multiresolution strategy, in which multiple scales of both image resolution and control point grid spacing are considered (Rueckert et al., 1999). In general, this strategy improves the result, allowing for larger deformations without being trapped in a local minimum.

In this work, a multiresolution framework is developed for XFFD, initializing the transformation with the output transformation from the previous scale. Since the transformations in two consecutive scales are represented by different sets of parameters, we need to obtain the mapping between the

parameter sets that renders the transformations themselves equivalent. We name this operation *parameter upsampling*.

~~Despite its importance, parameter upsampling has not received much attention in recent years. For instance, the multiresolution strategy employed in (Delmon et al. 2013) was not explained, although it is not straightforward, since the B-spline transformation parameters need to be decomposed into normal and tangential directions, which vary across different resolutions.~~ Despite its importance, parameter upsampling has not received sufficient attention in the literature. To the best knowledge of the authors, this process has not been explicitly described in details and and only sometimes the reader is referred to one of the following articles (Unser et al., 1993a,b; Forsey and Bartels, 1988). Nevertheless, its application in the case of methods in which discontinuous motion is represented is not straightforward.

In the literature, there are two existing strategies for parameter upsampling: least square approximation (Unser et al., 1993a,b), and B-spline refinement (Forsey and Bartels, 1988). The first method was initially designed for image resampling. But it is widely used for B-spline parameter upsampling, as it has been implemented in ITK (Ibanez et al., 2003) and employed in Elastix (Klein et al., 2010). However, it is not straightforward to extend it for XFFD. The second method was derived by (Forsey and Bartels, 1988) only for 2D, and with a notation not easily generalizable for other dimensions. In this work, we have followed the second strategy, but have reformulated it with more intuitive expressions, in order to develop its extension for XFFD in any dimension. We demonstrate that this procedure has a unique solution and integrates the formula in the multiresolution XFFD method.

In our previous work (Hua et al., 2015), a preliminary version of the XFFD method was presented with a sub-optimal multiresolution strategy, in which the moving image at a resolution is initialized using the warped image from the previous level. The method was described in outline with limited validation on sliding motion of a lung dataset and a synthetic case. In this article, we integrate XFFD into a rigorously formulated multiresolution framework based on parameter upsampling, and provide full details of the formulation. We further provide a much expanded validation study, not limited to sliding motion, encompassing experiments on a new synthetic dataset (representing free discontinuous motion, characteristic of objects that are non-attached and can move freely from each other), and a liver data set involving sliding motion and discontinuous free motion.

The remainder of this paper is structured as follows. In Section 2, we briefly present the conventional FFD formulation (Section 2.1), followed by that of XFFD, which integrates discontinuities by enriching B-spline basis functions (Section 2.2-2.3), and the multiresolution strategy integrating the parameter upsampling (Section 2.4). The datasets used for evaluation are depicted in Section 3. The description of the experiments and results in these datasets are presented in Section 4 and 5, respectively. We discuss the performance of the proposed methods and review its advantages and limitations in Section 6, followed by the conclusions in Section 7.

2. METHODS

2.1. Free form deformation

FFD was developed as a method to deform objects in computer graphics (Barr, 1984) and was later introduced to transform a moving image of any dimension n to a target one in nonrigid image registration (Rueckert et al., 1999). In order to obtain smooth and continuous deformations, B-splines are commonly used as basis functions. The displacement of any point $\boldsymbol{x} = (x_1, \ldots, x_n) \in \mathbb{R}^n$ is thus expressed as the linear combination

$$\boldsymbol{D}(\boldsymbol{x}) = \sum_{\boldsymbol{I} \in \mathcal{C}} B_{\boldsymbol{I}}(\boldsymbol{x}) \boldsymbol{\mu_I} \tag{1}$$

where the index $\boldsymbol{I} = (I_1, \ldots, I_n)$ runs along the set of control points, $\mathcal{C}$, distributed in a regular grid at positions $\boldsymbol{x}_I$, and $\boldsymbol{\mu}_I$ is the displacement of the corresponding control point. The basis functions are tensor products of 1D B-spline functions centered at each control point:

$$B_I(\boldsymbol{x}) \equiv B\left(\frac{\boldsymbol{x} - \boldsymbol{x}_I}{\boldsymbol{L}}\right) \equiv \prod_{i=1}^{n} \beta\left(\frac{x_i - x_{I,i}}{L_i}\right) \tag{2}$$

where L_i is the spacing between control points along the ith axis. The most used basis function is the cubic B-spline (Bankman, 2009),

$$\beta(u) = \begin{cases} \frac{2}{3} - \frac{1}{2}|u|^2(2 - |u|) & \text{if } |u| < 1 \\ \frac{1}{6}(2 - |u|)^3 & \text{if } 1 \leq |u| < 2 \\ 0 & \text{if } |u| \geq 2 \end{cases} \tag{3}$$

which is a symmetric C^2-differentiable piece-wise cubic function.

2.2. Extended free form deformation

The eXtended Free Form Deformation (XFFD) method has been inspired by the eXtended Finite Element methods (XFEM) (Fries and Belytschko, 2010). Because of the continuity of the standard FEM interpolation functions, discontinuities like fractures and material interfaces can only be incorporated by using a mesh that conforms to the interface geometry. Modelling evolving discontinuities therefore entails continuous remeshing, to maintain conformation with the changing interface geometry, incurring high computational cost. The XFEM avoids remeshing by adding an additional structure describing the location of the discontinuity surface, such as a surface mesh or level sets, and enriched basis functions encoding the desired discontinuities. In this work, we adopt a surface mesh to represent the discontinuity location and enrich the B-spline basis functions to incorporate discontinuities in the registration.

In a registration framework, discontinuities can be accommodated in a similar way to XFEM by introducing an enrichment term in the conventional FFD formalism (Hua et al., 2015):

$$\boldsymbol{D}(\boldsymbol{x}) = \sum_{\boldsymbol{I} \in \mathcal{C}} B_{\boldsymbol{I}}(\boldsymbol{x}) \boldsymbol{\mu_I} + \sum_{\boldsymbol{J} \in \widetilde{\mathcal{C}}} M_{\boldsymbol{J}}(\boldsymbol{x}) \boldsymbol{\lambda_J} \tag{4}$$

where $\boldsymbol{\lambda_J}$ denotes the parameters for the extra degrees of freedom, added for the subset of control points $\boldsymbol{J} \in \widetilde{\mathcal{C}}$, for which the discontinuity intersects the support of their corresponding basis function, $B_{\boldsymbol{J}}(\boldsymbol{x})$. Since the extra degrees of freedom are added only near the discontinuities, the increase in computation with respect to standard FFD is not substantial. The enriched

10

basis function is defined by the product

$$M_{\boldsymbol{J}}(\boldsymbol{x}) = B_{\boldsymbol{J}}(\boldsymbol{x})\,\psi(\boldsymbol{x}) \tag{5}$$

where $\psi(\boldsymbol{x})$ is the enrichment function incorporating the discontinuity.

2.3. Enrichment function

The enrichment function must incorporate a gap across the discontinuity surface, but be continuous elsewhere. This can be implemented in many different ways. In general, we will consider an n-dimensional closed hypersurface, representing the boundary of an object. Then, the most simple option is the sign function

$$\psi(\boldsymbol{x}) = \begin{cases} -1 & \text{if } \boldsymbol{x} \text{ is inside} \\ 1 & \text{if } \boldsymbol{x} \text{ is outside} \end{cases} \tag{6}$$

An illustration of the resulting enriched basis functions, $M_{\boldsymbol{J}}(x)$, is presented in Fig. 1. Thus, the enriched basis functions decay to zero smoothly at the function support limits. This similarly guarantees a smooth transition between enriched and conventional control points, without introducing extra discontinuities. In addition, the L^p-norm (for any p) of these enriched functions coincides with that of the normal B-splines, and is independent of the control point. Observe that the enriched subset, $\widetilde{\mathcal{C}}$, only includes control points whose support region intersects with the discontinuity. The enriched function for control points outside this subset would be unavailing.

2.4. Control points upsampling

The most common strategy for the upsampling of the control points grid is to halve the grid spacing at each scale refinement, keeping all the control points in the same position and inserting extra control points between

(a)   (b)

(c)   (d)
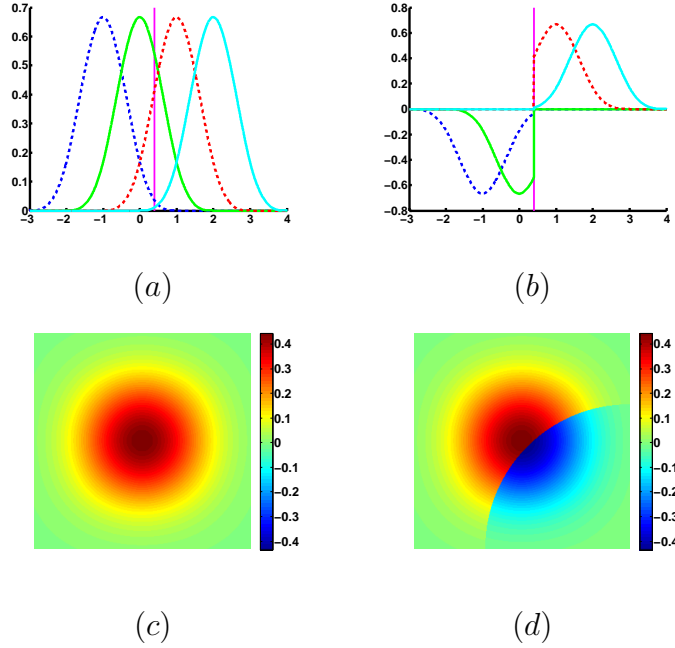
Figure 1: Enriched B-spline basis functions in the vicinity of a discontinuity, indicated by a dashed line: (a) conventional basis functions; (b) enriched basis functions. (c) a 2D conventional B-spline basis function; (d) a 2D enriched B-spline basis function with curved discontinuity boundary.

them. For this upsampling protocol, we prove below that a unique exact solution exists for the upsampling of the XFFD parameters, and we deduce the corresponding mapping. An analogous proof could be provided for the corresponding protocol of dividing the control points spacing by any integer m. However, for simplicity, we restrict the proof to $m = 2$.

Cubic B-splines are piecewise cubic polynomials. As stated in formula (3), the support of $\beta(u)$ is split into four components, corresponding to the intervals between consecutive control points: [-2,-1], [-1,0], [0,1], and [1,2].

The upsampled basis functions are also piecewise cubic polynomials for intervals resulting from halving the previous ones. It is evident that if a function is a cubic polynomial in an interval, it is also a cubic polynomial in any subinterval, with smooth matching between subintervals. This fact provides the intuition behind the result that the function $\beta(u)$ can be exactly represented as a linear combination of the upsampled basis:

$$\beta(u) = \sum_{k=-2}^{2} A_k \, \beta(2u - k) \tag{7}$$

Separating the equation into different intervals and expanding the expressions according to (3) results in a system of linear equations for the constants A_k, with polynomial coefficients in u. Although this system is overdetermined, it is consistent and has the unique solution

$$A_{-2} = A_2 = \frac{1}{8}, \quad A_{-1} = A_1 = \frac{1}{2}, \quad A_0 = \frac{3}{4}. \tag{8}$$

The resulting linear combination is illustrated in Fig. 2 (a). The symmetry of the coefficients is a consequence of the symmetry of the B-spline function.

Considering the definition of n-dimensional B-spline basis functions in (2), it is straightforward to derive the analogous expression for the upsampled basis functions:

$$
\begin{aligned}
B_{\boldsymbol{I}}(\boldsymbol{x}) &= \prod_{i=1}^{n} \beta\left(\frac{x_i - x_{I,i}}{L_i}\right) \\
&= \sum_{k_1=-2}^{2} \cdots \sum_{k_n=-2}^{2} \prod_{i=1}^{n} A_{k_i} \, \beta\left(2\frac{x_i - x_{\boldsymbol{I},i}}{L_i} - k_i\right)
\end{aligned} \tag{9}
$$

Since the control points are located in a regular grid with spacings $\boldsymbol{L} = (L_1, \ldots, L_n)$, their position can be expressed relative to the origin of the
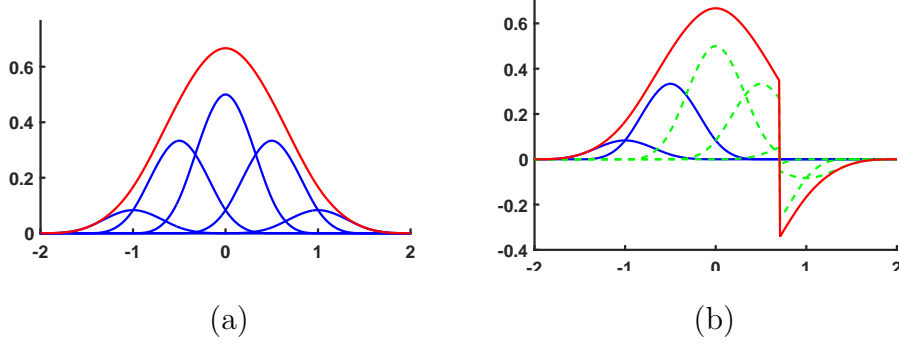
13

Figure 2: 1D B-spline basis functions, represented by the ones in the upsampled grid with half grid spacing: (a) a non-enriched B-spline basis function in the original grid (red) can be represented by non-enriched basis functions in the upsampled grid (blue); (b) an enriched B-spline basis function in the original grid (red) can be represented by non-enriched basis functions (blue) and enriched ones (green dashed line) in the upsampled grid.

control point grid: $\boldsymbol{x_I} = \boldsymbol{x_0} + \boldsymbol{IL}$. To simplify expressions we can assume $A_k = 0$ for $|k| > 2$, and denote $A_{\boldsymbol{k}} = A_{k_1} \times \cdots \times A_{k_n}$. Thus,

$$
\begin{aligned}
B_{\boldsymbol{I}}(\boldsymbol{x}) &= \sum_{\boldsymbol{k}} A_{\boldsymbol{k}} \prod_{i=1}^{n} \beta\left(\frac{x_i - x_{0,i}}{L_i/2} - 2I_i - k_i \right) \\
&= \sum_{\boldsymbol{k}} A_{\boldsymbol{k}} B^*_{2\boldsymbol{I}-\boldsymbol{k}}(\boldsymbol{x}) \\
&= \sum_{\boldsymbol{I}^* \in \mathcal{C}^*} A_{\boldsymbol{I}^*-2\boldsymbol{I}} B^*_{\boldsymbol{I}^*}(\boldsymbol{x}),
\end{aligned}
\tag{10}
$$

where we denote the upsampled functions, coefficients and sets by the superscript $*$.

The expression of the enriched basis functions (5) can be obtained from the previous one:

$$
M_{\boldsymbol{J}}(\boldsymbol{x}) = B_{\boldsymbol{J}}(\boldsymbol{x})\,\psi(\boldsymbol{x}) = \sum_{\boldsymbol{I}^* \in \mathcal{C}^*} A_{\boldsymbol{I}^*-2\boldsymbol{J}} B^*_{\boldsymbol{I}^*}(\boldsymbol{x})\,\psi(\boldsymbol{x})
\tag{11}
$$

14

In this summation, we need to discriminate between enriched and non-enriched control points. For the enriched ones, $\boldsymbol{J}^* \in \widetilde{\mathcal{C}}^*$, the product of the upsampled basis functions with $\psi(\boldsymbol{x})$ results in the upsampled enriched basis functions, $M_{\boldsymbol{J}^*}^*(\boldsymbol{x})$. For the non-enriched ones, $\boldsymbol{I}^* \in \mathcal{C}^* \setminus \widetilde{\mathcal{C}}^*$, the factor $\psi(\boldsymbol{x})$ is constant in the whole support of the function $B_{\boldsymbol{I}^*}^*(\boldsymbol{x})$, being positive or negative depending on the region where the control point, $\boldsymbol{x}_{\boldsymbol{I}^*}$, is located. Thus, we obtain

$$M_{\boldsymbol{J}}(\boldsymbol{x}) = \sum_{\boldsymbol{I}^* \in \mathcal{C}^*} S_{\boldsymbol{I}^*} A_{\boldsymbol{I}^* - 2\boldsymbol{J}} B_{\boldsymbol{I}^*}^*(\boldsymbol{x}) + \sum_{\boldsymbol{J}^* \in \widetilde{\mathcal{C}}^*} A_{\boldsymbol{J}^* - 2\boldsymbol{J}} M_{\boldsymbol{J}^*}^*(\boldsymbol{x}), \qquad (12)$$

where

$$S_{\boldsymbol{I}^*} = \begin{cases} -1 & \text{if } \boldsymbol{x}_{\boldsymbol{I}^*} \text{ is inside and } \boldsymbol{I}^* \notin \widetilde{\mathcal{C}}^* \\ 1 & \text{if } \boldsymbol{x}_{\boldsymbol{I}^*} \text{ is outside and } \boldsymbol{I}^* \notin \widetilde{\mathcal{C}}^* \\ 0 & \text{if } \boldsymbol{I}^* \in \widetilde{\mathcal{C}}^*. \end{cases} \qquad (13)$$

Fig. 2 (b) illustrates this linear combination for the enriched functions.

We can now substitute (10) and (13) into (4) to reexpress the displacements in the upsampled basis functions:

$$\boldsymbol{D}(\boldsymbol{x}) = \sum_{\boldsymbol{I}^* \in \mathcal{C}^*} B_{\boldsymbol{I}^*}^*(\boldsymbol{x}) \boldsymbol{\mu}_{\boldsymbol{I}^*} + \sum_{\boldsymbol{J}^* \in \widetilde{\mathcal{C}}^*} M_{\boldsymbol{J}^*}^*(\boldsymbol{x}) \boldsymbol{\lambda}_{\boldsymbol{J}^*} \qquad (14)$$

where the upsampled parameters are

$$\boldsymbol{\mu}_{\boldsymbol{I}^*} = \sum_{\boldsymbol{I} \in \mathcal{C}} A_{\boldsymbol{I}^* - 2\boldsymbol{I}} \, \boldsymbol{\mu}_{\boldsymbol{I}} + \sum_{\boldsymbol{J} \in \widetilde{\mathcal{C}}} S_{\boldsymbol{I}^*} A_{\boldsymbol{I}^* - 2\boldsymbol{J}} \, \boldsymbol{\lambda}_{\boldsymbol{J}}$$

$$\boldsymbol{\lambda}_{\boldsymbol{J}^*} = \sum_{\boldsymbol{J} \in \widetilde{\mathcal{C}}} A_{\boldsymbol{J}^* - 2\boldsymbol{J}} \, \boldsymbol{\lambda}_{\boldsymbol{J}} \qquad (15)$$

Observe that enriched and non-enriched parameters are coupled in the upsampling.

3. Materials

To evaluate the proposed method, one synthetic dataset and two publicly available datasets were employed for validation:

3.1. Synthetic dataset

The first dataset includes two 2D images with checkerboard texture and a deformation pattern that emulates sliding motion. The image size is 256×256 pixels. In the target image, the right-side region was vertically displaced by 15 pixels (Fig. 4).

The second synthetic dataset presents free discontinuous motion. The images show two objects that touch and separate, with resolution of 512×512 pixels (Fig. 7). The target image is composed of four elements, two circles touching each other and two small ellipses near the right circle. The moving image differs from the target in that the right circle moves towards the right side and the two ellipses towards each other. The right circle can move independently of the other structures and the surrounding materials. Thus, the discontinuity interface was set at its boundary.

3.2. DIR-lab dataset

The dataset contains 10 4D CT images acquired from patients treated for esophageal and lung cancer with a spatial resolution varying between $0.97 \times 0.97 \times 2.5$ mm^3 and $1.16 \times 1.16 \times 2.5$ mm^3 (Castillo et al., 2009). This dataset includes 300 landmarks for each image volume annotated by experts with inter-observer variability around 1 mm (Castillo et al., 2009). Lung masks were semi-automatically created using thresholding and morphological operations followed by manual corrections.

3.3. 4D CT liver ~~images~~ dataset

This dataset consists of 4 cases acquired in the Children's National Medical Center at Stanford (Pace et al., 2013). The images cover the lower part of the lungs and abdominal organs, including the liver. For each volume, 20 landmarks were provided for the abdominal organs. A rough segmentation of the liver was also provided for each volume. The mask for the target image was manually corrected and used as input of XFFD.

For both medical image datasets, the volume at the end of inhale was selected as the target image and the one at the end of exhale as the moving image.

In the respiratory cycle, the lungs exhibit sliding motion at the lung boundary against the rib cage and diaphragm, as the lungs expand and contract, while the ribs and spine remain relatively static (Fig. 3 (a-b)). The liver motion is more complicated, as it is the most movable abdominal organ (Suramo et al., 1983), and does not have a fixed relationship to the skin surface or the surrounding organs (Clifford et al., 2002; Siva et al., 2013), although they are related by ligaments or membranes (O'Rahilly and Müller, 1983). Thus, the liver can be subject to both sliding and free discontinuous motion (Fig. 3 (c-d)).

4. Experiments

The proposed method has been implemented as a module in the image registration toolbox Elastix (Klein et al., 2010). In our experiments, we employed XFFD as the transformation model and adopted normalized cross-correlation as similarity metric, and Limited memory Broyden-Fletcher-Goldfarb-
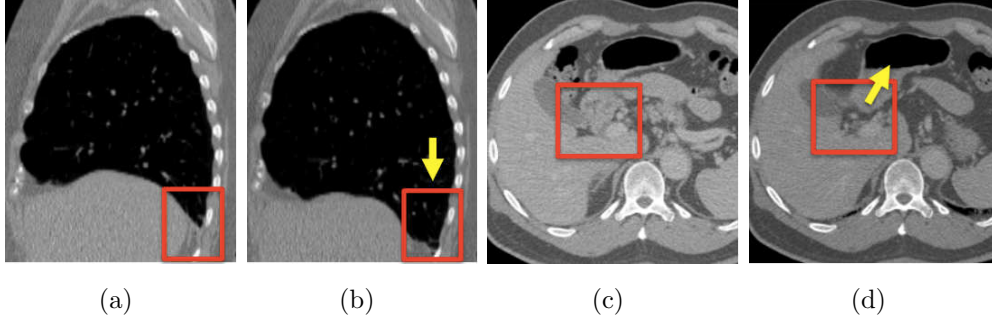
Figure 3: Motion ~~of~~ in the clinical datasets: (a-b) lung motion; (c-d) liver motion.

Shanno (LBFGS) as the optimizer, because cross-correlation is robust to linear variations in image intensity (Penney et al., 1998) and LBFGS is known for its high performance in dealing with high-dimensional problems (Zhu et al., 1997). For the sake of fair comparison, we selected similar parameters to the previous work in (Berendsen et al., 2014). For the lung and liver datasets, five scales were employed in the multiresolution scheme. At each resolution, the image was smoothed and downsampled by a Gaussian smoothing pyramid with standard deviation (σ) corresponding to half of the one at the previous scale. For the five scales, we set $\sigma = (16, 8, 4, 2, 1)$ voxels in the transversal plane and $\sigma = (8, 4, 2, 1, 0)$ voxels in the perpendicular direction, since the transversal image spacing is approximately half of that of the vertical. The grid spacing was set to be (80, 80, 40, 20, 10) mm for each scale. For the first synthetic dataset, a single resolution was employed with grid spacing of 64×64 pixels. For the second synthetic dataset, three resolutions were used with grid spacings 256, 128, and 64 pixels.

4.1. Metrics for evaluation

Target Registration Error (TRE) was employed to quantitatively evaluate the accuracy of the registration. We computed the Euclidean distance between the landmarks in the moving image and those in the target image, displaced by the deformation field. The mean and standard deviation of the distance of all the landmarks in each case was reported as the TRE ~~Target Registration Error (TRE)~~ (Schmidt-Richberg et al., 2012; Pace et al., 2013; Papież et al., 2014; Wu et al., 2008; Delmon et al., 2013; Berendsen et al., 2014).

Gap and Overlap volumes may appear between the regions in both sides of the discontinuity as an undesired effect, when dealing with discontinuities in the transformation. To evaluate this effect, the surface mesh describing the discontinuity interface was transformed by considering it to belong to either the inside or the outside, producing two transformed meshes, denoted as S^- and S^+, respectively. The volume enclosed by each transformed mesh was extracted and represented as a binary mask in the same resolution as registered images. This results in interior, $V_{\mathrm{In}}^{\pm}$, and exterior, $V_{\mathrm{Out}}^{\pm}$, regions for each surface, $S^{\pm}$. Then, the gap volume were measured as $V_{\mathrm{Out}}^- \cap V_{\mathrm{In}}^+$ and the overlap volume as $V_{\mathrm{In}}^- \cap V_{\mathrm{Out}}^+$ (Wu et al., 2008; Delmon et al., 2013; Berendsen et al., 2014).

Qualitative evaluation of the resulting deformation field was performed by visual inspection of the transformed grid and the displacement vector field. Plausibility of the tissue expansion and compression was assessed by the volumetric strain, which is computed from the determinant of the Jacobian of the transformation (Brannon, 2008).

4.2. Comparison between FFD and XFFD: influence of incorporating discontinuous transformations

To evaluate the importance of handling discontinuities in image registration, qualitative evaluation was performed in the synthetic images presenting sliding motion and DIR-lab dataset for both XFFD and FFD. In both datasets, the resulting transformed images, deformation field and volumetric strain field were visualized and compared.

Qualitative comparison between FFD and XFFD was also performed on the second synthetic dataset, presenting free discontinuous motion, by visualizing the transformed grid.

4.3. Comparison with previous methods

Multiresolution XFFD was compared with previous methods tested in the two clinical datasets. The DIR-lab dataset was adopted in most of the previous methods treating discontinuities. We computed the same measurements, TRE, gap and overlap volumes, as reported in all the B-spline based methods (Wu et al., 2008; Delmon et al., 2013; Berendsen et al., 2014) and some diffusion-based methods (Schmidt-Richberg et al., 2012; Pace et al., 2013; Papież et al., 2014).

For a fairer comparison, we also benchmarked XFFD against two previous methods (Wu et al., 2008; Delmon et al., 2013) using the same parameters and lung masks employed for XFFD on the DIR-lab dataset. We re-implemented Wu's method (Wu et al., 2008) and employed the implementation of Delmon's method (Delmon et al., 2013) in Elastix (Klein et al., 2010).

In the second synthetic dataset, presenting free discontinuous motion, we demonstrate that the proposed method is not restricted to sliding motion.

This is complemented by the evaluation of the TRE in the liver dataset, subject to complex discontinuous motion in the abdomen. The results were compared with the two previous methods tested on the same dataset (Risser et al., 2013; Papież et al., 2014), which handle sliding motion. Gap and overlap volumes were not relevant in this dataset, since some organs separate from the liver and sliding motion does not exist everywhere at the discontinuity interface.

5. Results

5.1. Comparison between FFD and XFFD: influence of incorporating discontinuous transformations

In the synthetic dataset presenting sliding motion, XFFD produced a more accurate transformed image than FFD, as the latter introduced artifacts, especially near the discontinuity (Fig. 4). The displacement field and transformed grid demonstrated that the discontinuities in the deformation field have been properly handled by XFFD, while FFD failed to do so. The displacements obtained from XFFD showed uniform rigid movement at the right side of the image, while the displacements were almost zero at the left side. This was in agreement with the actual deformation in the synthetic images. On the contrary, FFD generated artifacts in the displacement field near the discontinuity, which also influenced a larger neighbourhood. These errors in the deformation field can be propagated in quantities computed from the displacements, such as strain. The ideal strain field of this experiment should be zero across the whole image, as there is only rigid motion. However, because of its inability to treat discontinuities, FFD produced an

unphysical volumetric strain field, in which the maximum value was 36.52, compared to 0.10 obtained from XFFD.

For the second synthetic dataset, the resulting transformed grid showed XFFD is able to handle free discontinuous motion, while FFD produced an unrealistic transformation (Fig. 7).

Similar results were obtained in the DIR-lab dataset (Fig. 5). XFFD showed the expected discontinuities in the deformation field, visible in the transformed grid. This is in agreement with the relatively large motion of the lungs and the very small vertical movement of the rib cage observed in the images. In contrast, for FFD, the transformed grid evidences artifacts near the discontinuity boundaries, as a result of imposing continuity indiscriminately. By properly handling discontinuities, XFFD avoided unphysical strains, which were present FFD results. The maximum volumetric strain was 1037.32 in FFD, compared to 1.75 in XFFD. The color map in the figure was trimmed to the range [-1,5] for visualization.

5.2. Comparison with previous methods

In the DIR-lab dataset, the TRE obtained with multiresolution XFFD was better than those of all previous methods in every subject (Table 1). The average TRE was 1.17mm, improving the best previous results by 14.0%. The resulting gap and overlap volumes were reasonable. Compared with the best previous method, the overlaps were reduced by 50%, but the gap volume was 22% larger (Table 2). Nevertheless, they correspond to an average surface-to-surface distance of 1.04 mm (standard deviation 1.09 mm) between the transformed meshes S^+ and S^-, which is comparable to the image resolution (1x1x2.5 mm^3).

Table 1: The mean and standard deviation of TRE in the DIR-lab dataset in comparison with other methods (mm)

Case	Before registration	Schmidt-Richberg (2012)	Pace (2013)	Papież (2014)	Wu (2008)	Delmon (2013)	Berendsen (2014)	$XFFD$
1	3.89 ± 2.78	1.22 ± 0.64	1.06 ± 0.57	1.05 ± 0.6	1.1 ± 0.5	1.2 ± 0.6	$\mathbf{1.00 \pm 0.52}$	$\mathbf{1.00 \pm 0.51}$
2	4.34 ± 3.90	1.14 ± 0.65	1.45 ± 1.00	1.08 ± 0.6	1.0 ± 0.5	1.1 ± 0.6	1.02 ± 0.57	$\mathbf{0.99 \pm 0.59}$
3	6.94 ± 4.05	1.36 ± 0.81	1.88 ± 1.35	1.49 ± 0.9	1.3 ± 0.7	1.6 ± 0.9	1.14 ± 0.89	$\mathbf{1.12 \pm 0.64}$
4	9.83 ± 4.86	2.68 ± 2.79	2.04 ± 1.40	1.90 ± 1.3	1.5 ± 1.0	1.6 ± 1.1	1.46 ± 0.96	$\mathbf{1.44 \pm 1.03}$
5	7.48 ± 5.51	1.57 ± 1.23	2.73 ± 2.13	1.99 ± 1.7	1.9 ± 1.5	2.0 ± 1.6	1.61 ± 1.48	$\mathbf{1.37 \pm 1.35}$
6	10.9 ± 6.97	2.21 ± 1.66	2.72 ± 2.04	2.36 ± 1.9	1.6 ± 0.9	1.7 ± 1.0	1.42 ± 0.89	$\mathbf{1.26 \pm 1.04}$
7	11.0 ± 7.43	3.81 ± 3.06	4.59 ± 3.41	2.32 ± 1.9	1.7 ± 1.1	1.9 ± 1.2	1.49 ± 1.06	$\mathbf{1.12 \pm 0.67}$
8	15.0 ± 9.01	3.42 ± 4.25	6.22 ± 5.69	3.58 ± 3.4	1.6 ± 1.4	2.2 ± 2.3	1.62 ± 1.71	$\mathbf{1.18 \pm 1.22}$
9	7.92 ± 3.98	1.83 ± 1.19	2.32 ± 1.42	1.74 ± 1.0	1.4 ± 0.8	1.6 ± 0.9	1.30 ± 0.76	$\mathbf{1.14 \pm 0.64}$
10	7.30 ± 6.35	2.06 ± 1.92	2.82 ± 2.50	2.02 ± 2.1	1.6 ± 1.2	1.7 ± 1.2	1.50 ± 1.31	$\mathbf{1.08 \pm 0.82}$
mean	8.46 ± 5.48	2.13 ± 1.82	2.78 ± 2.96	1.95 ± 0.7	1.47 ± 0.96	1.66 ± 1.14	1.36 ± 0.99	$\mathbf{1.17 \pm 0.85}$

Table 2: Gap/Overlap volumes in DIR-lab dataset in comparison with other methods (cm^3)

Case	Wu (2008)	Delmon (2013)	Berendsen (2014)	XFFD
1	38 / 26	39 / 15	$\mathbf{23}$ / 18	39 / $\mathbf{2}$
2	78 / 46	$\mathbf{67}$ / 60	74 / 34	74 / $\mathbf{31}$
3	99 / 28	83 / 33	$\mathbf{57}$ / 30	71 / $\mathbf{24}$
4	75 / 34	$\mathbf{66}$ / 44	$\mathbf{66}$ / 28	92 / $\mathbf{13}$
5	110 / 38	78 / 52	61 / 32	$\mathbf{54}$ / $\mathbf{6}$
6	$\mathbf{100}$ / 86	119 / 77	130 / 50	155 / $\mathbf{11}$
7	$\mathbf{105}$ / 79	108 / 77	119 / 45	138 / $\mathbf{19}$
8	96 / 91	92 / 93	$\mathbf{85}$ / 53	150 / $\mathbf{40}$
9	61 / 34	$\mathbf{54}$ / 44	70 / 51	58 / $\mathbf{14}$
10	120 / 63	$\mathbf{94}$ / 56	80 / 43	109 / $\mathbf{28}$
mean	88.2/52.5	80.0/55.1	$\mathbf{76.5}$/37.4	94.0/ $\mathbf{18.8}$

The TRE and gap and overlap volumes obtained from the methods in (Wu et al., 2008) and (Delmon et al., 2013), but using the same parameters and lung masks used for XFFD, are shown in Table 3. Both methods showed an improvement in the TRE compared to their reported results, but were still surpassed by XFFD. Wu's method also improved in the gap and overlap volumes. In contrast, Delmon's method showed a large increase in gap and overlap volumes, illustrating the limitation of the method in handling discontinuities with non-smooth shapes.

Table 3: The average TRE and gap and overlap volumes using the same parameters, compared with (Wu et al., 2008) and (Delmon et al., 2013).

	Wu (2008)	Delmon (2013)	XFFD
TRE (mm)	1.36 ± 1.61	1.38 ± 1.49	1.17 ± 0.85
gap/overlap (cm^3)	53.7/65.7	279.1/438.5	94.0/18.8

Similarly, in the liver dataset, the TRE obtained from XFFD improved on those from the two previous methods tested on the same dataset (Table 4), reducing the average TRE by 13% with respect to the best previous result. The obtained XFFD transformations are illustrated in Fig. 6 by the resulting grid deformation.

6. Discussion

Handling discontinuities in the deformation field is challenging. Attempts to address this issue have been based on direction-dependent or spatially varying regularisers (Schmidt-Richberg et al., 2012; Pace et al., 2013; Ruan et al., 2009; Heinrich et al., 2013; Papież et al., 2014), multiple B-spline trans-

Table 4: The mean and standard deviation of TRE in the 4D CT liver dataset (mm)

Case	Before registration	Pace (2013)	Papież (2015)	XFFD
0	9.08 ± 2.89	2.06 ± 1.10	N/A	$\mathbf{1.54 \pm 0.87}$
1	5.89 ± 3.15	2.10 ± 1.23	N/A	$\mathbf{1.56 \pm 0.93}$
2	6.30 ± 2.76	2.55 ± 1.41	N/A	$\mathbf{2.25 \pm 1.28}$
4	4.42 ± 3.30	2.82 ± 1.92	N/A	$\mathbf{2.41 \pm 0.98}$
mean	6.64 ± 3.42	2.30 ± 1.45	2.19	$\mathbf{1.94 \pm 1.01}$

formations (Wu et al., 2008; Delmon et al., 2013), or introduction of penalty terms to reduce gaps and overlaps (Berendsen et al., 2014). In contrast to these methods, we propose to handle this problem in the transformation model, such that the discontinuities are implicitly incorporated into a single B-spline transformation, while retaining all the desirable properties of B-splines. The proposed method imposes no constraint on the shape of the discontinuity interface and can handle free discontinuous motion. Other types of discontinuities, such as sliding motion, can be considered as constrained versions of this general type, according to the specific motion properties.

To demonstrate the significance of treating discontinuities in the deformation field, comparison was performed between the proposed method and FFD in the synthetic and DIR-lab dataset. In the synthetic dataset, the deformation can be described by a rigid body translation, having zero strain across the whole image. XFFD produced accurate displacements, correctly reflecting the physical properties of the actual deformation field, while FFD introduced unacceptable artifacts. These deficiencies were similarly exposed in the experiments on the lung images (Section 5.1).

For the purpose of benchmarking against previous methods, XFFD has

been tested on two publicly available datasets of lungs and liver. In the lung dataset, the distribution of the average motion of the landmarks was 8.46 ± 5.58 mm. This represents large scale motion when compared to the small structures present in the lungs (airways), thus challenging the registration algorithm. Despite the complexity of the images, XFFD achieved high accuracy in both applications. The average TRE was 1.17 mm for the lung dataset and 1.94 mm for the liver images, which significantly improves on the performance of the previous methods handling discontinuities tested on the same datasets. The experiment comparing with some previous methods using the same parameters and lung mask as for XFFD highlighted the performance gain due to the transformation model, as all the other aspects of registration were set to be the same. It confirms that the proposed transformation model is the key element in the higher accuracy obtained with XFFD.

XFFD does not involve any explicit control of gaps and overlaps. However, by using a single transformation, any misalignment is penalized, as it increases the image dissimilarity measure. Thus, the gap and overlap volumes obtained from XFFD were comparable to or better than the ones obtained from previous methods using *ad hoc* restrictions.

In this article, we proposed a registration method, which handles discontinuities in the deformations. Different types of discontinuous motion can be observed in medical images, such as sliding motion, in which two organs are touching but not attached; and free discontinuous motion, where two organs are not attached and can touch and separate. Other types of discontinuities can also be observed, for instance in the interface between tumours and the

26

surrounding tissues, in which the two tissues are attached but having different material properties. To improve the performance in handling other types of discontinuities, different constraints or more specific enrichment functions can be included in the XFFD framework to adapt to the specific applications.

In particular, XFFD does not include any constraint or penalty on the activation or the value of the enriched coefficients, $\boldsymbol{\lambda_J}$. Their value is driven in the registration only by the image similarity metric. This could result in instabilities or spurious discontinuities due to image noise, especially in homogeneous regions. The XFFD method could be extended to incorporate in the cost function a penalty term controlling $\boldsymbol{\lambda_J}$. This penalty could also be made location-dependent, restricting the discontinuity in regions of the interface which are known or expected to have nearly continuous motion.

Furthermore, regularisers are sometimes included in FFD to impose desired properties of the deformations, such as bending energy or incompressibility penalties. The regularisers often require derivatives of the transformation, which can be computed analytically in FFD. This property is also shared by XFFD. Thus, the proposed method is a flexible framework allowing inclusion of prior knowledge of the deformations via regularisers. In addition, any of the extensions of the FFD registration proposed in the past, such as spatio-temporal (De Craene et al., 2012) and diffeomorphic registration (Rueckert et al., 2006), may be straightforwardly included in the proposed framework.

The computational complexity of XFFD is comparable to that of FFD. It only differs in that the enriched control points near the discontinuity interface have twice as many parameters as those in FFD. Thus, the number of extra

parameters depends on the size and shape of the discontinuity interface, and on the resolution. Since the computational cost of one iteration of LBFGS increases linearly with respect to the number of parameters (Zhu et al., 1997), the computational complexity of the XFFD is bounded to twice that of the FFD. In our experiments on the DIR-lab dataset, the average increase in the number of parameters across all the resolutions was 30%.

A limitation of XFFD is that it requires a segmentation in the target image. This requirement is, however, shared by all the other B-spline based methods (Wu et al., 2008; Delmon et al., 2013; Berendsen et al., 2014) and most of the diffusion-based methods (~~Schmidt-Richberg et al., 2012;~~ Risser et al., 2013; Pace et al., 2013). This may be facilitated by using an automatic segmentation method (Nakagomi et al., 2013; Tomoshige et al., 2014; Rebouças Filho et al., 2017) as a previous step. Extensions of the presented method to enable automatic detection of the discontinuity boundaries during registration, without prior segmentation, are subjects of current research.

7. Conclusion

In this article, we have developed a novel registration framework, coined XFFD, that handles discontinuous transformations that generally accompany tissue transitions. XFFD treats discontinuities within a single B-spline transformation, by enriching the basis functions to incorporate discontinuities across the considered tissue interfaces. We have also integrated XFFD into a multiresolution framework using parameter upsampling.

XFFD does not incorporate any ad hoc penalty term conforming to a particular type of deformation. It has been tested on synthetic images, 3D

lung and liver datasets along the respiratory cycle. The lungs follow sliding motion with respect to the rib cage, while the liver involves complex motions with respect to surrounding organs. In both datasets, XFFD showed high performance, compared to the state-of-the-art methods treating discontinuities tested on the same datasets.

References

Bankman, I.N., 2009. Handbook of Medical Image Processing and Analysis. Academic Press, 405–406.

Barr, A.H., 1984. Global and local deformations of solid primitives. ACM Siggraph Computer Graphics 18, 21–30.

Berendsen, F.F., Kotte, A.N., Viergever, M.A., Pluim, J.P., 2014. Registration of organs with sliding interfaces and changing topologies, in: SPIE Medical Imaging, International Society for Optics and Photonics. pp. 90340E–90340E.

Brannon, R., 2008. Kinematics: The mathematics of deformation. Course Notes, ME EN 6530, 10–10.

Castillo, R., Castillo, E., Guerra, R., Johnson, V.E., McPhail, T., et al., 2009. A framework for evaluation of deformable image registration spatial accuracy using large landmark point sets. Physics in Medicine and Biology 54, 1849–1870.

Clifford, M.A., Banovac, F., Levy, E., Cleary, K., 2002. Assessment of hep-

atic motion secondary to respiration for computer assisted interventions. Computer Aided Surgery 7, 291–299.

De Craene, M., Piella, G., Camara, O., Duchateau, N., Silva, E., Doltra, A., D'hooge, J., Brugada, J., Sitges, M., Frangi, A.F., 2012. Temporal diffeomorphic free-form deformation: Application to motion and strain estimation from 3D echocardiography. Medical Image Analysis 16, 427–450.

Delmon, V., Rit, S., Pinho, R., Sarrut, D., 2013. Registration of sliding objects using direction dependent B-splines decomposition. Physics in medicine and biology 58, 1303–1314.

Forsey, D.R., Bartels, R.H., 1988. Hierarchical B-spline refinement, in: ACM transitions on Computer Graphics, ACM. pp. 205–212.

Fries, T., Belytschko, T., 2010. The extended/generalized finite element method: an overview of the method and its applications. International Journal for Numerical Methods in Engineering 84, 253–304.

Heinrich, M.P., Jenkinson, M., Papież, B.W., Glesson, F.V., Brady, M., Schnabel, J.A., 2013. Edge-and detail-preserving sparse image representations for deformable registration of chest MRI and CT volumes, in: Information Processing in Medical Imaging, Springer. pp. 463–474.

Hua, R., Pozo, J.M., Taylor, Z.A., Frangi, A.F., 2015. Discontinuous nonrigid registration using extended free-form deformations, in: SPIE Medical Imaging, International Society for Optics and Photonics. pp. 94131P–94131P.

Ibanez, L., Schroeder, W., Ng, L., Cates, J., 2003. The ITK software guide .

Klein, S., Staring, M., Murphy, K., Viergever, M.A., Pluim, J.P., 2010. Elastix: a toolbox for intensity-based medical image registration. Medical Imaging, IEEE Transactions on 29, 196–205.

Mirsky, I., 1976. Assessment of passive elastic stiffness of cardiac muscle: mathematical concepts, physiologic and clinical considerations, directions of future research. Progress in cardiovascular diseases 18, 277–308.

Nakagomi, K., Shimizu, A., Kobatake, H., Yakami, M., Fujimoto, K., Togashi, K., 2013. Multi-shape graph cuts with neighbor prior constraints and its application to lung segmentation from a chest CT volume. Medical image analysis 17, 62–77.

O'Rahilly, R., Müller, F., 1983. Basic human anatomy: a regional study of human structure. WB Saunders Company.

Pace, D., Enquobahrie, A., Yang, H., Aylward, S., Niethammer, M., 2011. Deformable image registration of sliding organs using anisotropic diffusive regularization, in: ISBI IEEE International Symposium on, IEEE. pp. 407–413.

Pace, D.F., Aylward, S.R., Niethammer, M., 2013. A locally adaptive regularization based on anisotropic diffusion for deformable image registration of sliding organs. Medical Imaging, IEEE Transactions on 32, 2114–2126.

Papież, B.W., Heinrich, M.P., Fehrenbach, J., Risser, L., Schnabel, J.A., 2014. An implicit sliding-motion preserving regularisation via bilateral

filtering for deformable image registration. Medical image analysis 18, 1299–1311.

Penney, G.P., Weese, J., Little, J., Desmedt, P., Hill, D.L., Hawkes, D.J., et al., 1998. A comparison of similarity measures for use in 2-D-3-D medical image registration. Medical Imaging, IEEE Transactions on 17, 586–595.

Piella, G., De Craene, M., Butakoff, C., Grau, V., Yao, C., Nedjati-Gilani, S., Penney, G.P., Frangi, A.F., 2013. Multiview diffeomorphic registration: Application to motion and strain estimation from 3D echocardiography. Medical image analysis 17, 348–364.

Rebouças Filho, P.P., Cortez, P.C., da Silva Barros, A.C., Albuquerque, V.H.C., Tavares, J.M.R., 2017. Novel and powerful 3D adaptive crisp active contour method applied in the segmentation of CT lung images. Medical Image Analysis 35, 503–516.

Risser, L., Vialard, F.X., Baluwala, H.Y., Schnabel, J.A., 2013. Piecewise-diffeomorphic image registration: Application to the motion estimation between 3D CT lung images with sliding conditions. Medical image analysis 17, 182–193.

Ruan, D., Esedoglu, S., Fessler, J.A., 2009. Discriminative sliding preserving regularization in medical image registration, in: ISBI, IEEE. pp. 430–433.

Rueckert, D., Aljabar, P., Heckemann, R.A., Hajnal, J.V., Hammers, A., 2006. Diffeomorphic registration using B-splines, in: International Conference on Medical Image Computing and Computer-Assisted Intervention, Springer. pp. 702–709.

Rueckert, D., Sonoda, Luke, I., Hayes, C., Hill, Derek, L.G., Leach, M.O., Hawkes, D.J., 1999. Nonrigid registration using free-form deformations: application to breast MR images. Medical Imaging, IEEE Transactions on 18, 712–721.

Schmidt-Richberg, A., Werner, R., Handels, H., Ehrhardt, J., 2012. Estimation of slipping organ motion by registration with direction-dependent regularization. Medical Image Analysis 16, 150–159.

Siva, S., Pham, D., Gill, S., Bressel, M., Dang, K., Devereux, T., Kron, T., Foroudi, F., 2013. An analysis of respiratory induced kidney motion on four-dimensional computed tomography and its implications for stereotactic kidney radiotherapy. Radiat Oncol 8, 248.

Suramo, I., Päivänsalo, M., Myllylä, V., 1983. Cranio-caudal movements of the liver, pancreas and kidneys in respiration. Acta radiologica: diagnosis 25, 129–131.

Tomoshige, S., Oost, E., Shimizu, A., Watanabe, H., Nawano, S., 2014. A conditional statistical shape model with integrated error estimation of the conditions; application to liver segmentation in non-contrast CT images. Medical image analysis 18, 130–143.

Unser, M., Aldroubi, A., Eden, M., 1993a. B-spline signal processing. I. Theory. Signal Processing, IEEE Transactions on 41, 821–833.

Unser, M., Aldroubi, A., Eden, M., 1993b. B-spline signal processing. II. Efficiency design and applications. Signal Processing, IEEE Transactions on 41, 834–848.

Wu, Z., Rietzel, E., Boldea, V., Sarrut, D., Sharp, G.C., 2008. Evaluation of deformable registration of patient lung 4DCT with subanatomical region segmentations. Medical physics 35, 775–781.

Zhu, C., Byrd, R.H., Lu, P., Nocedal, J., 1997. Algorithm 778: L-BFGS-B: Fortran subroutines for large-scale bound-constrained optimization. ACM Transactions on Mathematical Software (TOMS) 23, 550–560.
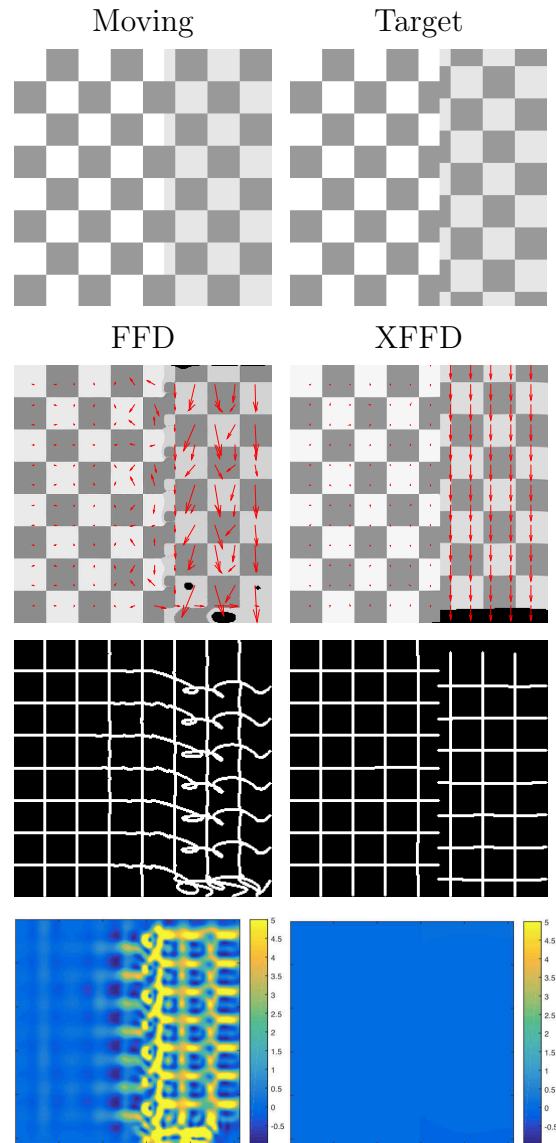
Figure 4: Results in synthetic dataset with sliding motion: moving and target image; 2nd row: transformed images overlaid with displacement fields obtained from FFD and XFFD; 3rd row: transformed grid obtained from FFD and XFFD; 4th row: strain fields obtained from FFD and XFFD. The color map in the figure was trimmed to the range [-1,5] for visualization.
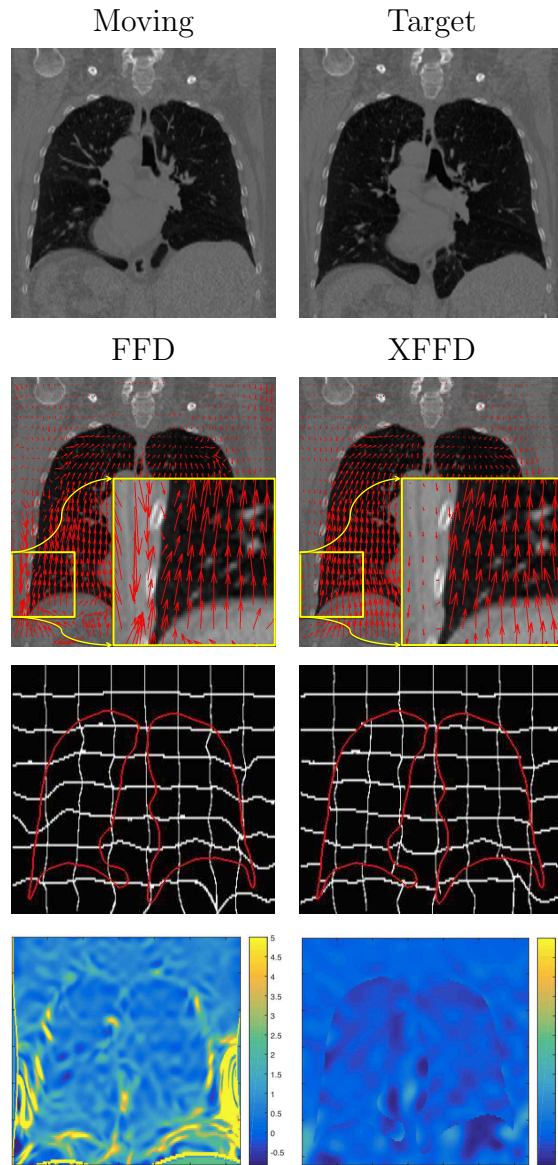
Figure 5: Qualitative results in DIR-lab dataset for sliding motion: 1st row: moving and target image; 2nd row: transformed images overlaid with displacement fields obtained from FFD and XFFD; 3rd row: transformed grid obtained from FFD and XFFD, surface mesh of discontinuity (red); 4th row: strain fields obtained from FFD and XFFD. The color map in the figure was trimmed to the range [-1,5] for visualization, although the maximum value for FFD was 1037.32, compared to 1.75 in XFFD.

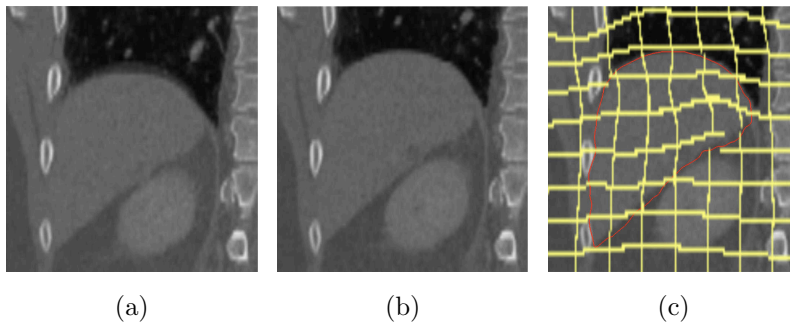(a)   (b)   (c)

Figure 6: Transformed grid in the liver dataset: (a) moving image; (b) target image; (c) transformed grid overlay on moving image with liver boundary in red.
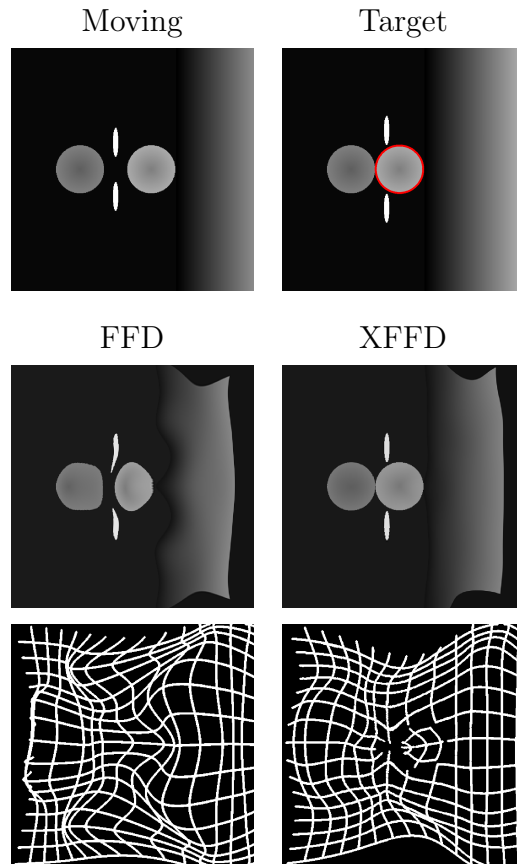
Figure 7: Results in synthetic dataset for free discontinuous motion: 1st row: moving image and target image with discontinuity interface (red); 2nd row: transformed images obtained with FFD and XFFD; 3rd row: transformed grid obtained from FFD and XFFD.